Enhancement of Upconversion Emission of LaPO4:Er@Yb Core−Shell Nanoparticles/Nanorods

6 AUTHORS, INCLUDING:

Pushpal Ghosh
Dr. Harisingh Gour University
20 PUBLICATIONS 581 CITATIONS

SEE PROFILE

Krishna Kanta Haldar
Central University of Punjab
16 PUBLICATIONS 398 CITATIONS

SEE PROFILE

David Octavio Solis
Zizala Lighting Systems
16 PUBLICATIONS 260 CITATIONS

SEE PROFILE

Amitava Patra
Indian Association for the Cultivation of Sci…
172 PUBLICATIONS 4,135 CITATIONS

SEE PROFILE

Article

Enhancement of Upconversion Emission of LaPO:Er@Yb Core#Shell Nanoparticles/Nanorods

Pushpal Ghosh, Jorge Oliva, Elder De la Rosa, Krishna Kanta Haldar, David Solis, and Amitava Patra

More About This Article

Additional resources and features associated with this article are available within the HTML version:

- Supporting Information
- Access to high resolution figures
- Links to articles and content related to this article
- Copyright permission to reproduce figures and/or text from this article

View the Full Text HTML

Enhancement of Upconversion Emission of LaPO₄:Er@Yb Core−Shell Nanoparticles/Nanorods

Pushpal Ghosh,[†] Jorge Oliva,[‡] Elder De la Rosa,[‡] Krishna Kanta Haldar,[†] David Solis,[‡] and Amitava Patra*,[†]

Department of Materials Science & Centre for Advanced Materials, Indian Association for the Cultivation of Science, Kolkata 700 032, India, and Centro de Investigaciones en Optica, A.P. 1-948, León Gto. 37160, México

We demonstrated the synthesis of LaPO₄:Er:Yb-doped nanoparticles/nanorods and LaPO₄:Er@Yb core−shell nanoparticles/nanorods by a solution-based technique. The mechanism related to morphology control of LaPO₄: Er:Yb nanorods/nanoparticles is proposed and discussed. Bright-green (550 nm) and red (670 nm) emission were observed due to the transitions $^2H_{11/2} + {}^4S_{3/2} \rightarrow {}^4I_{15/2}$ and $^4F_{9/2} \rightarrow {}^4I_{15/2}$, respectively. The experimental data for 550- and 670-nm emission bands of doped nanoparticle/nanorod and core−shell nanoparticles/nanorods have been fit with a straight line with a slope of ∼2, which confirms the two-photon absorption process. The enhancement of upconversion emission of LaPO₄:Er:Yb-doped nanoparticles and LaPO₄:Er@Yb core−shell nanoparticles/nanorods are mainly due to modifications of surface-related effects. It is found that the tensile strain increases from +1.0% to +1.9% with changing the shape from nanoparticle to nanorod and reversal of the lattice strain (compressive) is obtained for coated nanoparticle/ nanorod. It is worth mentioning that the lattice strain varies with changing the shape and surface coating on nanocrystals and the upconversion emission intensity increases with decreasing the tensile lattice strain and it increases with increasing compressive strain. Analysis suggests that the lattice strain plays an important role in modification of the upconversion properties of the rare-earth-doped nanocrystals.

Introduction

Rare-earth-doped upconverted nanocrystals have shown great promise as a new class of materials for photonic and biophotonic applications.[1] Intensive research efforts are therefore devoted to designing and tuning of the upconversion properties of trivalent rare-earth-ion-doped nanocrystals.[2–4] The synthesis and spectroscopy of upconverting nanoparticles have recently garnered considerable attention because of their potential use as biolabels and in biological assays.[5,6] Güdel et al.[7] reported blue, green, and red upconversion emission from lanthanide-doped LuPO₄ and YbPO₄ nanocrystals in a transparent colloidal solution. This recent developments in water-soluble luminescent lanthanide nanoparticles and upconverting lanthanide phosphors have proven to be novel strategies for designing highly luminescent and photostable lanthanide nanoprobes.[7] Recently, Caruso and co-workers[8] have demonstrated the biofunctionalization of rare-earth-doped lanthanum phosphate colloidal nanoparticles. As luminescence probes, the main advantage of upconverting nanoparticles is that the interference of background noises with luminescence detection can be avoided because they have an excitation wavelength at 980 nm and short emission wavelengths in the visible light range, while no biological matrix upconverts in the infrared range. Therefore, upconverting nanoparticles can be expected to develop new assay platforms for more bioassay applications.[6] The applications of these nanoparticles to bioimaging and biochip technologies will be an emerging field. Because these potential applications are still

very much in the design-phase; further fundamental research in this field remains a challenge. It is already reported that the crystal phase, size, and concentration play important roles on the upconversion emission properties of rare-earth-doped nanocrystals.[9] Much attention has already been paid to Eu³⁺-doped LaPO₄ nanocrystals also.[10] However, there is no study on the influence of the shape and core−shell structure of Er³⁺:Yb³⁺-doped LaPO₄ nanoparticles on their upconversion emission properties, to our knowledge. Core−shell particles have been attracting a great deal of interest to improve the luminescence efficiency by reducing the surface defects of the nanocrystals. It is important to investigate how the lattice strain changes with changing the shape and surface coating of nanoparticles and their effect on the upconversion emission properties. Generally, dopant ions substitute metal ions of the host lattice in doped materials. However, in the case of coated nanoparticles, surface enrichment of the dopant ions may tune the optical properties due to different local site symmetries. Hasse et al.[11] reported the quantum yield enhancement from 53% for CePO₄:Tb nanoparticles to 80% for CePO₄:Tb/LaPO₄ core−shell nanoparticles. They attributed the significant enhancement of the quantum yield to core−shell nanoparticles due to suppressing energy-loss processes at the nanoparticle surface. Main motivation of this work is to synthesis of LaPO₄:Er:Yb-doped nanoparticles/nanorods and LaPO₄:Er@Yb core−shell nanoparticles/nanorods and try to understand the influence of surface coating and shape on the upconversion emission properties. Here, we use a solution-based process "soft chemistry" for making controlled nanostructure materials. Of particular interest is how the other physical properties of these materials vary with the modification of the shape and surface coating with the hope that such knowledge will enable us to construct efficient

* Author to whom correspondence should be addressed. E-mail: msap@iacs.res.in. Phone: (91)-33-2473-4971. Fax: (91)-33-2473-2805.
† Indian Association for the Cultivation of Science.
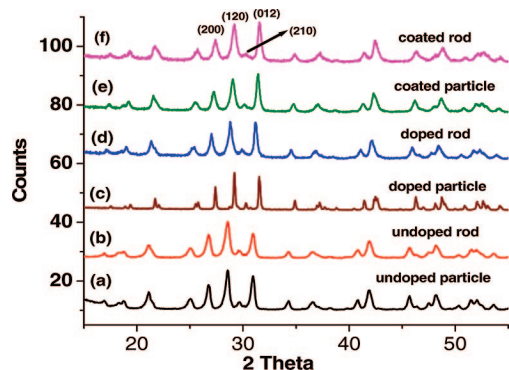‡ Centro de Investigaciones en Optica.

LaPO₄:Er@Yb Core−Shell Nanoparticles/Nanorods

J. Phys. Chem. C, Vol. 112, No. 26, 2008 **9651**

Figure 1. XRD patterns of undoped, doped, and coated LaPO₄ nanoparticles/nanorods prepared at 900 °C.
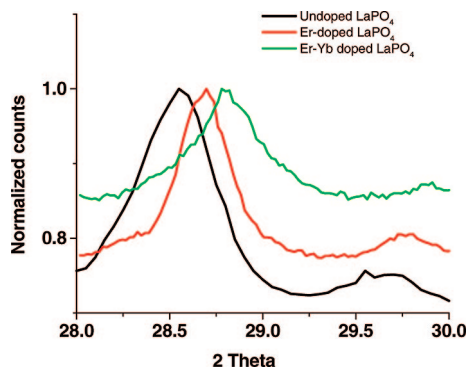

Figure 2. Normalized XRD patterns of undoped, 1 mol % Er³⁺-doped, 1 mol % Er³⁺-, and 1 mol % Yb³⁺-doped LaPO₄ nanoparticles prepared at 900 °C.

nanomaterials. Lattice strain may vary with changing the shape and surface coating of the nanoparticles, which might effect the upconversion emission properties. The fundamental question that we are attempting to address in this paper is how the shape and core−shell structure cause any noticeable change on the upconversion emission properties of LaPO₄:Er:Yb-doped nanoparticles/nanorods and LaPO₄:Er@Yb core−shell nanoparticles/nanorods. The morphologies, structure, formation mechanism, and upconversion emission properties of these nanocrystals are investigated in detail.

Experimental Procedures

A simple wet chemical method and hydrothermal method were employed to prepare doped and coated nanoparticle and nanorod samples.

Preparation of LaPO₄:Er:Yb-Doped Nanoparticles. In the present study, we use a water-in-oil (w/o)-type emulsion for preparing these nanocrystals. Here, the nanoreactor was prepared through a water-in-oil (w/o)-type emulsion with cyclohexane and sorbitan monooleate (Span 80, Fluka) as the organic liquid phase (oil phase) and nonionic surfactant, respectively, with a low hydrophilic−lyophilic balance number of 4.3. The support solvent containing 5 vol % of Span 80 in cyclohexane was used for emulsification. Then, 0.085 (M), 10 mL aqueous solution of La(NO₃)₃·6H₂O (Lobachemie) was added to the above explained microemulsion and stirred for 5 min followed by dropwise addition of 0.085 (M) 10 mL solution of H₃PO₄ (85% pure, Merck). The entire solution is stirred for 5 min at room temperature. The pH of the solution varies from 2 to 3. Finally, the required amount of 5 mL of erbium nitrate and 5 mL of ytterbium nitrate solution (for 1 mol % Er₂O₃ and 1.0 mol % Yb₂O₃) were added to the mixed solution, and the whole solution

was stirred for 30 min. Then, a sufficient amount of acetone was added in it and stirred for 30 min. Finally, a white precipitate was obtained. Particles were then collected by centrifugation (6000 rpm), and then the particles were washed twice with acetone and methanol and dried at 60 °C for 12 h in a vacuum oven. Finally, the samples were heated at 900 °C in air for 1 h with a rate of heating of 2 °C/min.

Preparation of LaPO₄:Er:Yb Nnanorods. Considering the important role played by CTAB in determining the morphology of the nanomaterials, we used this cationic surfactant to prepare rod-shaped LaPO₄ nanocrystals. Here, 10 mL 0.085 (M) aqueous solution of La(NO₃)₃·6H₂O and 10 mL 0.085 (M) H₃PO₄ solution were added together under stirring conditions followed by the addition of the required amount of erbium nitrate and ytterbium nitrate solution (for 1 mol % Er₂O₃ and 1.0 mol %Yb₂O₃). Then, 20 mL of aqueous solution of 0.017 (M) cetyl trimethyl ammonium bromide (CTAB) (ALFA AESAR) was added to the solution. The pH of the solution was checked, and it is in between 2 and 3. Then the mixture was transferred into a Teflon-lined stainless-steel autoclave of 100 mL capacity, sealed, and maintained at 120 °C for 3 h followed by natural cooling to room temperature. Finally, the white precipitate was washed, collected, and heated at 900 °C.

Preparation of Core−Shell LaPO₄:Er@Yb Nanoparticles/ Nanorods. To prepare core−shell LaPO₄:Er@Yb nanoparticles, the required amount of 1 mol % Er³⁺-doped LaPO₄ nanoparticles was taken in a beaker with 30 mL of water and sonicated for 1 h in an open beaker kept in an ice bath. After sonication, the required amount of ytterbium nitrate (1.0 mol %) solution was added to it and stirred for 5 min followed by dropwise addition of NH₄OH (v/v = 1:1) solution to maintain the pH at 8−9. The resulting product was washed extensively with water, centrifuged, and dried under vacuum. Finally, the white precipitate was washed, collected, and heated at 900 °C. A similar method was also employed to prepare LaPO₄:Er@Yb nanorods. Here, 1 mol % Yb₂O₃ is used for coating with the 99% LaPO₄:Er core material. The particles are well dispersed in water and ethanol.

Transmission electron microscopy (TEM, JEOL Model 200) was used to study the morphology and particle size of the resulting powders. The crystalline phases of the heated powders were identified by X-ray diffraction (XRD) using a Siefert XRD 3000 P. The crystallite sizes of the nanocrystals were calculated following Scherrer's equation

$$D = \frac{K\lambda}{\beta \cos \theta} \qquad (1)$$

where $K = 0.94$, D represents crystallite size (Å), λ is the wavelength of Cu Kα radiation, and β is the corrected half-width of the diffraction peak.

Optical Characterization. Infrared spectra of the powders (FTIR) were recorded in the range 400−4000 cm⁻¹ on a Fourier transformation spectrometer (Nicolet Magna IR 750 Series 2). A small amount of sample is mixed with KBr and then pressed to make a thin pellet for FTIR studies. The photoluminescence (PL) characterization was carried out using a 300 mW CW laser diode LDD-9A (from ATC semiconductor devices) centered at 970 nm. The fluorescence emission was analyzed with an Acton Research modular 2300 spectrofluorometer, a R955 Hamamatsu photomultiplier tube for visible emission, and an InGaAs photodetector for NIR emission. All photoluminescence measurements were done at room temperature.

9652 *J. Phys. Chem. C, Vol. 112, No. 26, 2008*

Ghosh et al.

TABLE 1: Phase Compositions, Crystallite Sizes, and Cell Parameters of Doped and Coated LaPO$_4$ Nanoparticles and Nanorods

sample name	temp (°C)	crystal phase	crystallite size (nm) (±1.5 nm)	cell parameter (Å)	cell volume (Å^3)	lattice strain (%)
undoped LaPO$_4$ nanoparticle	900	monoclinic	20.2	$a = 6.8560$ $b = 7.1483$ $c = 6.5790$	313.35	0.35
undoped LaPO$_4$ nanorod	900	monoclinic	17.3	$a = 6.8713$ $b = 7.1067$ $c = 6.5257$	310.03	1.20
Er^{3+}-doped LaPO$_4$: nanoparticle	900	monoclinic	22.4	$a = 6.8245$ $b = 7.1072$ $c = 6.5512$	308.79	0.48
Er^{3+}:Yb^{3+} doped LaPO$_4$: nanoparticle	900	monoclinic	48.3	$a = 6.7009$ $b = 6.9988$ $c = 6.5142$	297.23	1.00
Er^{3+} doped LaPO$_4$: nanorod	900	monoclinic	20.2	$a = 6.8392$ $b = 7.0673$ $c = 6.4946$	305.34	1.64
Er^{3+}:Yb^{3+} doped LaPO$_4$: nanorod	900	monoclinic	23	$a = 6.7819$ $b = 7.0272$ $c = 6.4787$	300.55	1.90
core−shell LaPO$_4$:Er@Yb nanoparticles	900	monoclinic	19.9	$a = 6.7482$ $b = 6.9823$ $c = 6.4478$	295.73	−0.37
core−shell LaPO$_4$:Er@Yb nanorods	900	monoclinic	18.7	$a = 6.7246$ $b = 6.9614$ $c = 6.4449$	293.53	−0.19

Results and Discussion

Structural Investigations. Figure 1 depicts the XRD pattern of 900 °C heated undoped, doped, and coated LaPO$_4$ nanoparticles/nanorods. The phase composition, crystallite size, and cell parameter as a function of doping and surface coating are summarized in Table 1. Figure 1a shows the XRD pattern of 900 °C heated undoped LaPO$_4$ nanoparticles. The strong peaks at 21.06° (101), 26.75° (200), 28.54° (120), 29.64° (210), and 30.94° (012) clearly indicate the formation of a monoclinic monazite structure (JCPDS card no 32-493) having space group $P_{21/n}$ (14). It is well-known[12] that the lanthanide atoms are coordinated with nine oxygen atoms forming a polyhedron of pentagonal interpenetrating tetrahedrons in the monoclinic structure. Again, these nine coordinated lanthanide atoms form a chain by combining with distorted tetrahedrayl PO$_4^{3-}$ groups. Using Scherrer's equation, the average crystallite size is 20.2 nm, calculated from the peak at 28.54°. The measured lattice parameters are $a = 6.8560$ Å, $b = 7.1483$ Å, $c = 6.5790$ Å, and the unit cell volume is 313.35 Å^3 (see Table 1). Figure 1b shows the XRD pattern of a 900 °C heated undoped LaPO$_4$ nanorod. All peaks are well indexed with monoclinic monazite phase, and the crystallite size is 17.3 nm. It is seen from Table 1 that the lattice parameter c changes from 6.525 to 6.579Å with changing shape from a nanorod to a nanoparticle. Zhang et al.[13] described that the growth of LaPO$_4$ nanorods or nanowires can be done either along the [001] (c axis) or [100] (a axis) direction. From the thermodynamic viewpoint, the growth along the [001] direction can release more energy than that along the [100] plane.[12] The c value of the nanorod is lower than that of the nanaoparticle samples; therefore, we may say that the anisotropic growth occurs along the c axis in the nanorod samples. Figure 1c depicts the XRD pattern of 900 °C heated LaPO$_4$:Er:Yb-doped nanoparticles. The peaks at 21.65° (101), 27.35° (200), 29.16° (120), 30.2° (210), and 31.43° (012) are well-indexed with monoclinic phase. The measured lattice

parameters are $a = 6.7009$ (Å), $b = 6.9988$ (Å), $c = 6.5142$(Å), and the unit cell volume is 297.227 (Å^3). The XRD pattern depicted by Figure 1d is for 900 °C heated LaPO$_4$:Er:Yb-doped nanorod samples. The peaks are well-indexed with the monoclinic monazite phase of LaPO$_4$. The cell parameters are listed in Table 1. It is seen (Table 1) that the cell parameters and cell volume of doped nanoparticle and nanorod samples are lower than those of undoped nanoparticle and nanorod samples. According to Vegard's law, the cell parameter decreases with increasing the dopant concentration.[14] Liang et al.[15] also reported that the cell parameter decreases with increasing Yb^{3+} concentration. This result indicates that both Er^{3+} and Yb^{3+} ions are incorporated into the monoclinic LaPO$_4$ nanoparticle and nanorod samples. Figure 1e and 1f depict the XRD pattern of the 900 °C heated core−shell LaPO$_4$:Er@Yb nanoparticles/ nanorods. Monoclinic phase is observed in both cases, and the crystallite sizes are 19.9 and 18.7 nm for the coated particle and rod shaped samples, respectively. It is interesting that the crystallite size of the coated samples is lower than that of the doped samples (both rod and particle). In the present study, the surface coating by Yb$_2$O$_3$ prevents self-aggregation or Ostwald ripening during the growth of LaPO$_4$ particles with increasing the temperature, whereas aggregation or Ostwald ripening occurred during the heating of doped materials at 900 °C. For this reason, surface modification leads to smaller particle sizes. The 100 intensity peak of cubic Yb$_2$O$_3$ is at 29.6° (JCPDS File no 41-1106). However, the (210) plane of monoclinic monazite of the LaPO$_4$ particle is also at 29.6°. Here, we used only 1 mol % Yb$_2$O$_3$ for the coating, which is much less compared to that of the core [99% LaPO$_4$:Er]. Therefore, it is very difficult to distinguish or obtain the peaks for Yb$_2$O$_3$. The formation of core−shell structured particles with Yb$_2$O$_3$ shell materials was confirmed by HRTEM images. The cell parameters for the coated samples are significantly lower than those of the doped material. The c values are 6.5071 and 6.449 Å for the doped
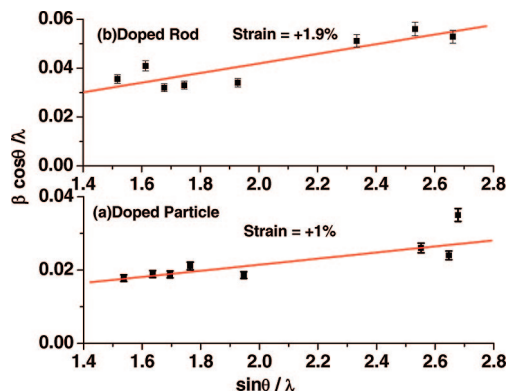
Figure 3. Plot of $\beta \cos \theta/\lambda$ against $\sin \theta/\lambda$ for 1 mol % Er^{3+}- and Yb^{3+}-doped particles (a) and rods (b) prepared at 900 °C.

Figure 4. Plot of $\beta \cos \theta/\lambda$ against $\sin \theta/\lambda$ for core−shell LaPO$_4$: Er@Yb nanoparticles (a) and rod prepared at 900 °C.

and coated samples, respectively. Therefore, it suggests that the surface coating plays an important role in tuning the crystalline size by controlling the crystal growth.

Figure 2 shows the shifting of the normalized XRD pattern of undoped, Er-doped, and Er-Yb doped nanoparticles prepared at 900 °C. The peak at 28.54° (120) is shifted to 28.67° from the undoped to the 1 mol % Er$_2$O$_3$-doped sample. This peak is further shifted to 28.80° for the Er^{3+}- and Yb^{3+}-doped samples. Here, we observed the shifting of the diffraction peak with increasing concentration. This gradual shifting of the diffraction line undoubtedly indicates the effective doping. A part of these dopant ions may incorporate in substitutional or interstitial sites of LaPO$_4$ after heating. Shah et al.[16] showed a slight shift of the diffraction peak of the TiO$_2$ particle to the smaller angles with increasing Nd^{3+} concentration, where the Nd^{3+} (0.983 Å) is much larger than the host Ti^{4+} (0.605 Å). The ionic radii of Er^{3+} (1.062 Å) and Yb^{3+} (1.042 Å) are much smaller (14%) than those of the nine coordinated La^{3+} (1.216 Å) ions.[17] Yu et al.[18] reported the substitution of La^{3+} ions by Sr^{2+}. So it is clear that the small sized Er^{3+} and Yb^{3+} can substitute the La^{3+} ion in LaPO$_4$.

Generally, the broadenings of the diffraction peaks depend upon two predominant factors, that is, strain and particle size. We calculate the strain using Williamson and Hall thereom[19]

$$\beta \cos \theta = 1/D + \eta \sin \theta/\lambda \qquad (2)$$

where β is the full width at half-maximum (fwhm), θ is the diffraction angle, λ is the X-ray wavelength, D is the effective particle size, and η is the effective strain. The strain is calculated from the slope, and the crystallite size (D) is calculated from the intercept of a plot of $\beta \cos \theta/\lambda$ against $\sin \theta/\lambda$. Figure 3a shows the plot of $\beta \cos \theta/\lambda$ against $\sin \theta/\lambda$ for LaPO$_4$:Er:Yb-doped nanoparticles. The positive slope value indicates the tensile strain. The tensile strain (+1.0%) is observed for LaPO$_4$: Er:Yb-doped nanoparticles, which is ~1.5 times larger than 1 mol % Er^{3+}-doped and ~3 times larger than undoped LaPO$_4$ particles (Supporting Information and Table 1). Tensile strain is defined as deformation along a line segment that increases in length when a load is applied along that line. Therefore, lattice strain can be tuned by doping. Figure 3b shows the plot for a LaPO$_4$:Er:Yb-doped nanorod. The observed tensile strain is +1.9%, which is larger than that of the 1 mol % Er^{3+}-doped nanorod and ~1.5 times larger than that of the undoped rod (Supporting Information and Table 1). It is worth mentioning that the tensile strain of the nanorod is higher than that of the nanoparticles (~2 times). Therefore, it reveals that lattice strain can be tuned by changing the shape of particles.
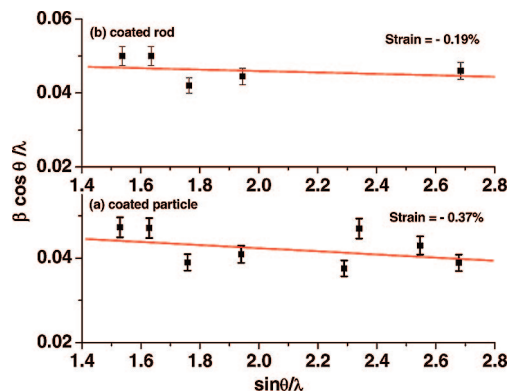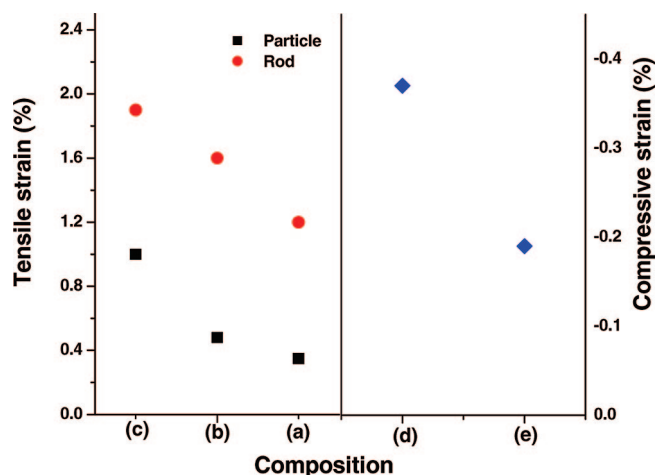

Figure 5. Plot of lattice strain against composition: (a) undoped LaPO$_4$ particle and rod, (b) 1 mol % Er^{3+}-doped LaPO$_4$ particle and rod, (c) 1 mol % Er^{3+}- and Yb^{3+}-doped LaPO$_4$ particle and rod, (d) core−shell LaPO$_4$:Er@Yb particles, and (e) core−shell LaPO$_4$:Er@ Yb rods.

Figure 4a shows the plot of $\beta \cos \theta/\lambda$ against $\sin \theta/\lambda$ for 900 °C heated core−shell LaPO$_4$:Er@Yb nanoparticles. The reversal of lattice strain is observed for coated samples. Here we get a negative slope (−0.0037), which suggests the presence of compressive strain (−0.37%), and crystallite size is 22 nm (from intercept), which is in good agreement with the calculated value from the Scherrer equation (Table 1). Compressive strain is defined as deformation along a line segment that decreases in length when a load is applied. We observed the tensile strain for doped LaPO$_4$ particle, whereas compressive strain is obtained after surface coating, which is an important observation of this study. A similar kind of observation was observed for the Eu^{3+}-coated TiO$_2$ particle[20]. Figure 4b shows the plot of $\beta \cos \theta/\lambda$ against $\sin \theta/\lambda$ for the 900 °C heated core−shell LaPO$_4$:Er@Yb nanorod. A negative slope, that is, compressive strain, is observed (−0.19%) in the coated nanorod sample. However, the tensile strain is obtained in the doped nanorod samples (Supporting Information Figures S2b and S3b). Analysis suggests that the lattice strain can also be tuned by surface coating, which is an important observation in this study. A summary of the results of the relation of lattice strain with changing dopant concentration, shape, and surface coating is shown in Figure 5. In summary, we can say that the tensile strain increases with increasing dopant concentration and the tensile strain of nanorod samples is higher than that of the nanoparticles. However, the compressive strain is observed for all coated samples.

The morphology and microstructural details can be obtained from the TEM study. Figure 6a shows the low-magnification
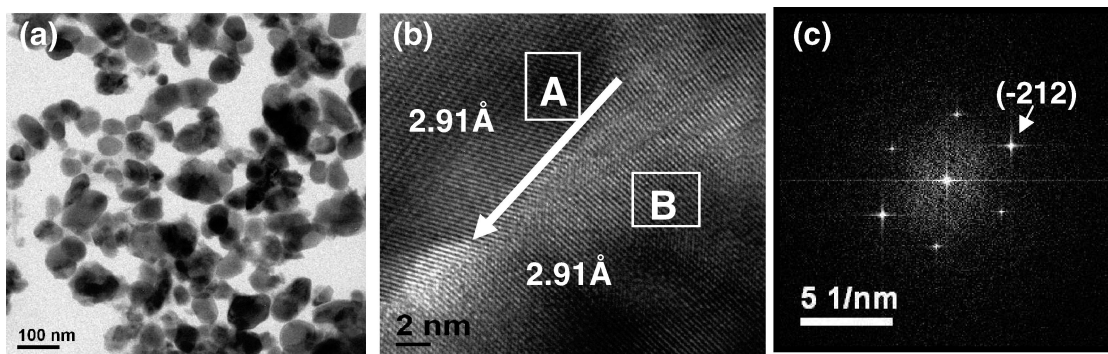
Figure 6. TEM micrographs (a) HRTEM (b) and SAED pattern (c) of 900 °C heated Er- and Yb-doped LaPO$_4$ nanoparticle.
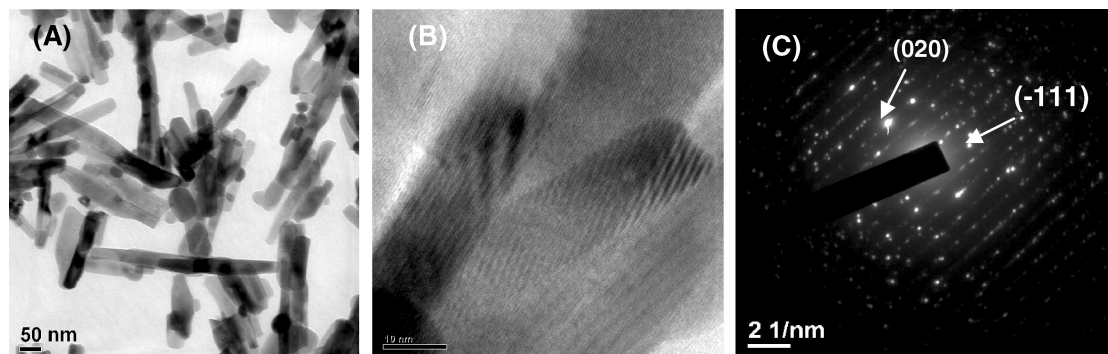

Figure 7. TEM micrograph (a) HRTEM (b) and SAED pattern (c) of 900 °C heated Er.

TEM images of 900 °C heated Er^{3+}:Yb^{3+}-doped LaPO$_4$ nanoparticles; the particles are normally spherical in shape, and the average size is 48 nm, which matches with the size obtained from XRD. Figure 6b shows the HRTEM image of this nanocrystal. The interplanar distance is 2.91 Å, which corresponds to the (012) plane of the monoclinic LaPO$_4$ nanoparticle for both areas A and B. The corresponding FFT analysis (Figure 6c) confirms the presence of the (−212), (012), and (−202) planes of the monoclinic LaPO$_4$ nanoparticle. It is already seen from the HRTEM picture that the particles are joined at a planar interface and nucleate side by side and coalesce during growth. Here, we believe that imperfect oriented attachment occurs via the (012) plane among the particles and these particles are separated by twin bouandaries.[20,21] Banfield et al.[21] already reported this kind of imperfect oriented attachment in TiO$_2$ nanoparticles. This dislocation is indicated by the arrow heads in Figure 6b. Therefore, we believe that the imperfect oriented attachment growth mechanism occurs during Er^{3+}:Yb^{3+}-doped LaPO$_4$ nanoparticle formation. However, a different growth mechanism is observed in the case of nanorod formation. Figure 7a depicts the low-magnification TEM image of the 900 °C heated Er^{3+}:Yb^{3+}-doped LaPO$_4$ nanorod. The average diameter of these nanorods is 33 nm. Figure 7b shows the HRTEM image of the nanorods; the measured lattice spacing is 4.16 Å, which corresponds to the (−111) plane of monoclinic monazite LaPO$_4$. Figure 7c shows the selected-area electron diffraction (SAED) pattern for this nanocrystal. The presence of the (−111), (020), (200), (101), and (120) planes again confirms the formation of monoclinic monazite LaPO$_4$ (JCPDS card no. 32-493). Here, the cationic surfactant CTAB plays an important role in controlling the shape. A diffusion-controlled growth process was proposed by Peng et al.,[23] to explain the growth of CdSe nanorods in solution. Fang et al.[24] also used the diffusion model to explain high anisotropic growth of LnPO$_4$ nanorods. In the present study, the surfactant head groups of CTAB are adsorbed on surface plane of LaPO$_4$ primary nuclei, resulting in the

blocking of the nuclei sides[25] and the chemical potential increases in the open or exposed facet. In contrast, the spatial localization of the enriching water molecules provides the necessary anisotropy for the formation of the LaPO$_4$ nanorod.[24] Figure 8a represents the HRTEM image of 900 °C heated core−shell LaPO$_4$:Er@Yb nanoparticles, which clearly represents the surface coating around the LaPO$_4$ nanoparticle. The difference in contrast between the inner and outer part confirms the surface coating. The measured lattice spacing of the outer part of this HRTEM image is 3.15 Å, which corresponds to the 100 intensity plane (222) of cubic Yb$_2$O$_3$ (JCPDS file no. 41-1106). From the diffraction spot of the FFT pattern (Figure 8b), the (222) and (400) planes of cubic Yb$_2$O$_3$ are confirmed. It is to be noted that we did not observe oriented attachment of nanoparticles in coated nanoparticles. This reveals that the growth mechanism in coated nanoparticles is different because of surface coating. Figure 8c represents the HRTEM image of 900 °C heated core−shell LaPO$_4$:Er@Yb nanorods. The lattice spacing of the inner part of the rod (region A) is 3.125 Å, which corresponds to the 100 intensity plane (120) of monoclinic monazite LaPO$_4$. The lattice spacing of the outer part of the rod (region B) is 2.46 Å, corresponding to the (400) plane of cubic Yb$_2$O$_3$. Similarly, the interplanar distance is 2.97 Å measured in region C, corresponding to the (222) plane of cubic Yb$_2$O$_3$. The FFT (Figure 8d) pattern of the inner part of the nanorod (region A) corresponds to the (120) plane of monoclinic monazite LaPO$_4$. It is again confirmed from the FFT pattern of the outer part (region B) that the cubic Yb$_2$O$_3$ phase is present (picture is not given).

Upconversion Properties. Figure 9a depicts the UPC luminescence of 900 °C heated LaPO$_4$:Er:Yb-doped nanoparticles and nanorods after being excited at 970 nm. We measured the UPC luminescence under identical conditions to compare their emission intensities. Bright-green (550 nm) and red (675 nm) emission were observed due to the transitions $^2H_{11/2} + {}^4S_{3/2} \rightarrow {}^4I_{15/2}$ and $^4F_{9/2} \rightarrow {}^4I_{15/2}$, respectively.[9] Upconversion emission

LaPO$_4$:Er@Yb Core−Shell Nanoparticles/Nanorods

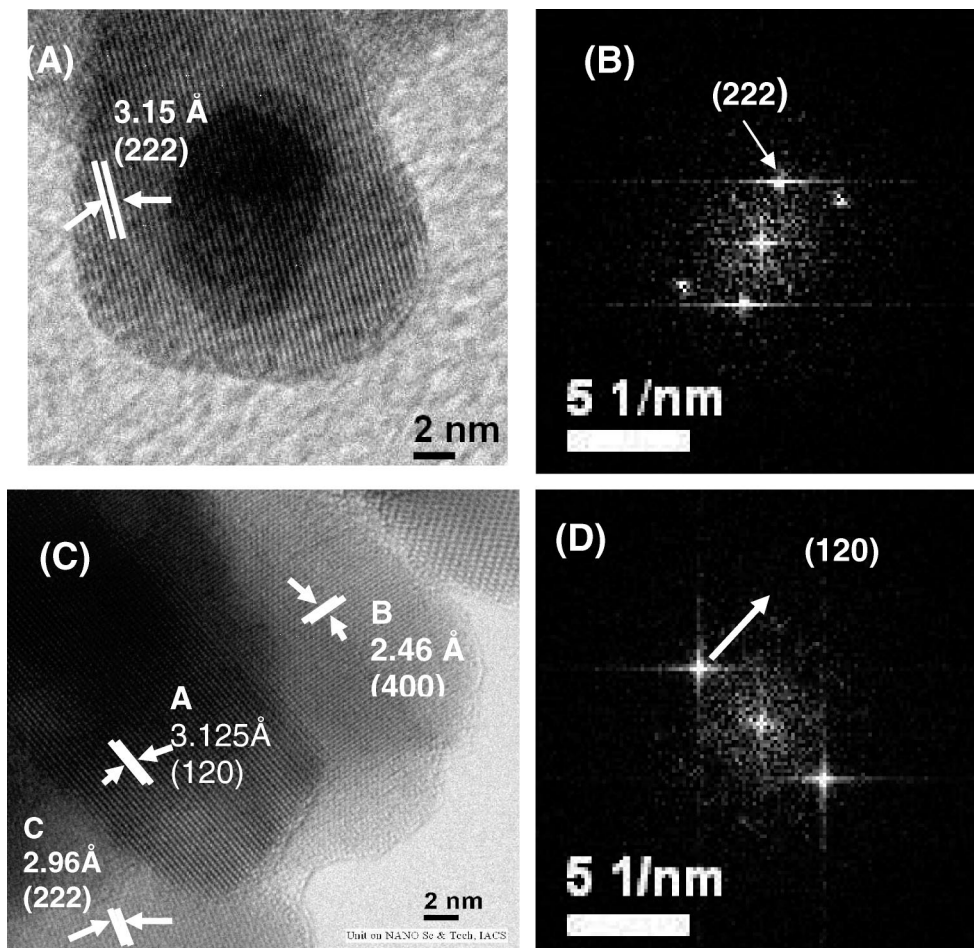*J. Phys. Chem. C, Vol. 112, No. 26, 2008* **9655**

Figure 8. HRTEM images of core−shell LaPO$_4$:Er@Yb nanoparticles (a), corresponding FFT pattern (b) nanorod (c) and corresponding FFT pattern (d).

bands at 525 and 550 nm are assigned to transitions from levels $^4H_{11/2}$ and $^4S_{3/2}$ to level $^4I_{15/2}$. The enhancement of upconversion emission intensity is observed in doped nanoparticles compared to doped nanorod samples. The relative intensity of green emission with respect to the intensity of red emission is 0.713 and 0.566 for nanoparticle and nanorod samples, respectively. This reveals that the efficiency of the upconversion property can be tuned with changing the shape of the particle.

Figure 9b shows the UPC luminescence of a 900 °C heated core−shell LaPO$_4$:Er@Yb nanoparticle and an LaPO$_4$:Er:Yb-doped nanoparticle after being excited at 970 nm. It is interesting to see the enhancement of upconversion emission intensity in core−shell samples compared to doped samples. Core−shell nanoparticles present the strongest emission of all of the studied samples and can be observed with the naked eye; see the inset in Figure 9b. The relative intensity of green emission with respect to the intensity of red emission is 0.909 and 0.485 for the core−shell nanoparticle and doped nanoparticles, respectively. It reveals that the core−shell structure also has a profound effect on the upconversion efficiency. Figure 9c shows the UPC luminescence of a 900 °C heated core−shell LaPO$_4$:Er@Yb nanorod and a LaPO$_4$:Er:Yb-doped rod after being excited at 970 nm. The fluorescence intensity is much stronger in core−shell nanorods than the intensity in the doped samples. The relative intensity of green emission with respect to the intensity of red emission is 0.485 and 0.566 for the core−shell rod and doped rod, respectively.

The mechanism of the upconverted emission of Er^{3+} has been well-established in the literature.[1,9] A typical energy-level diagram for the upconverted emission from a sample codoped with Yb^{3+} and Er^{3+} ions under infrared excitation is shown in Figure 10. Er^{3+} ions (acceptors) are excited by the energy transfer from the Yb^{3+} (donor) that are excited directly ($^2F_{5/2} \rightarrow {}^2F_{7/2}$) by the pumping signal. Direct excitation of Er is also possible; however, the energy transfer is most probably due to the larger absorption cross section of Yb and the resonance between $^2F_{5/2} \rightarrow {}^2F_{7/2}$ and $^4I_{15/2} \rightarrow {}^4I_{11/2}$ transitions of Yb and Er, respectively, as is shown in the energy diagram in Figure 10. Part of the $^4I_{11/2}$ excited ion relaxes nonradiatively to the $^4I_{13/2}$ level and from here relaxes to the ground state, producing the 1.532-μm emission band. And part was promoted to $^4F_{7/2}$ by the ET from the relaxation of another excited Yb or Er ($^4I_{11/2} \rightarrow {}^4I_{15/2}$) ion. The $^4F_{7/2}$ level decays nonradiatively to $^2H_{11/2} + {}^4S_{3/2}$ due to phonon energy. From here, the population decay to ground state producing bright-green emissions centered at 520 and 550 nm, respectively. And part decay nonradiatively to $^4F_{9/2}$ to finally decay to ground state ($^4F_{9/2} \rightarrow {}^4I_{15/2}$) producing the red emission centered at 670 nm. It is well-known for an unsaturated mechanism that the intensity of the upconverted luminescence, I_{upc}, is proportional to some power n of the excitation intensity I_i; that is, $I_{upc} = kI_i^n$, where $n = 2, 3, ...$ is the number of pump photons required to populate the emitting state and is determined from the slope of the line of the graph of intensity versus pump power in a log−log plot. In order to analyze the UPC mechanism, the pump power dependence of the green emission from $^4S_{3/2} \rightarrow {}^4I_{15/2}$ and red emission from the $^4F_{9/2} \rightarrow {}^4I_{15/2}$ level were investigated on excitation intensity at 970 nm for an Er^{3+}:Yb^{3+}-doped LaPO$_4$ nanoparticle and a
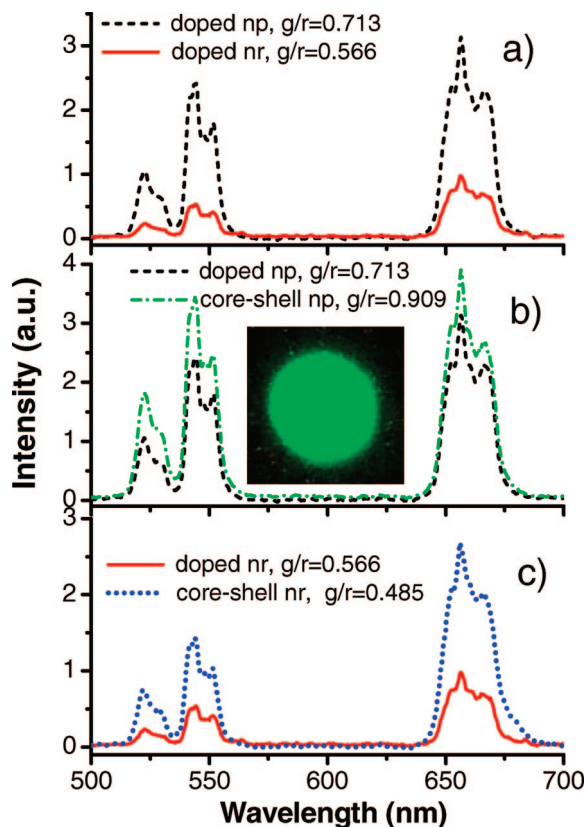
Figure 9. Upconversion emission of LaPO4:Er:Yb-doped and LaPO4:Er@Yb core−shell nanoparticles (np) and nanorods (nr). a−c present a comparison between different samples. The inset in b corresponds to the brilliant spot of luminescence obtained for core−shell nanoparticles.
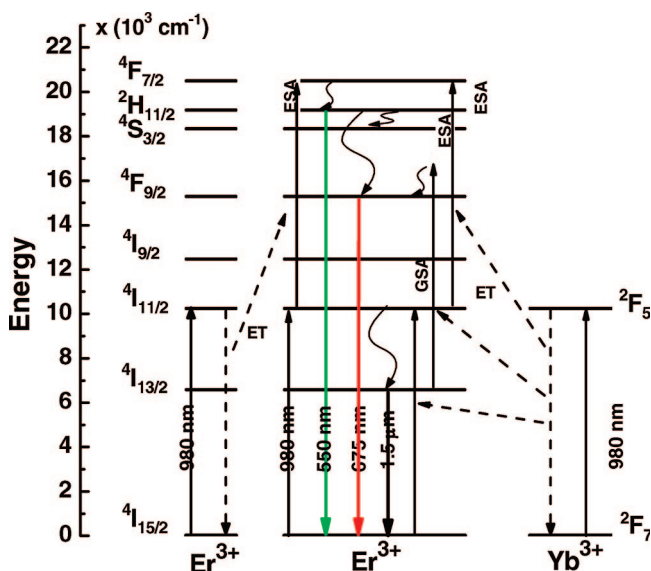

Figure 10. Energy diagram of the Yb−Er system describing the proposed mechanism responsible for the upconversion emission.

rod prepared at 900 °C; the results are shown in Figure 11a and b. The experimental data for 550- and 670-nm emission bands of doped nanoparticles and nanorods have been fitted with a straight line with a slope of ∼2, which confirms the two-photon absorption process. The experimental data for 550- and 670-nm emission bands of core−shell nanoparticles and rods (Figure 11c and d) have been fitted with a straight line with a slope of ∼2, which confirms that these UPC emission lines are also a two-photon absorption process.
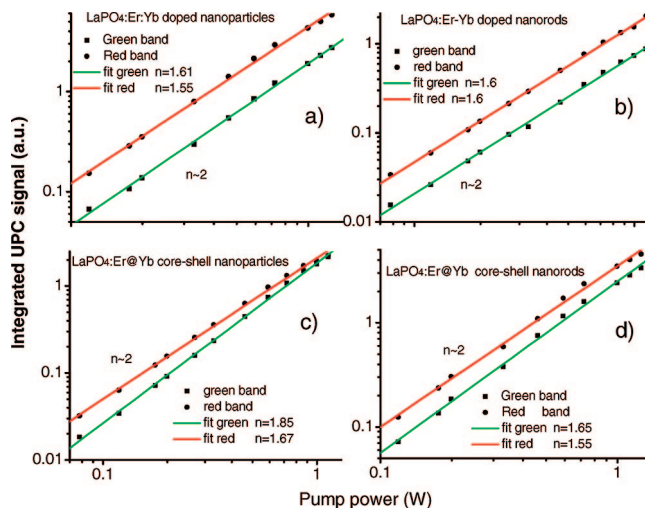

Figure 11. Integrated upconverted signal as function of pump power for both doped and core−shell nanoparticles (a and c) and nanorods (b and d).

The enhancement of the upconversion emission intensities in doped nanoparticles compared to doped nanorod samples is ascribed by two main factors: One factor is due to a change in surface area with changing shape, which induces the change of the number of surface defects in the host; and the second is the surface hydroxyl groups. Both factors influence the nonradiative relaxation rate.[3a] The surface area of a spherical nanoparticle is 82406.16 nm^3 (using $4/3\pi r^3$; $r = 27$ nm) where the surface area of the nanorod is 512919 nm^3 (using $4\pi r^2 h$, $r = 16.5$ nm and $h = 150$ nm). Because the surface area of the nanorods is much higher than that of the nanoparticles, the surface defects or the number of rare-earth ions on the surface are increased in the nanorod samples. In a normal crystal, the surface does not influence the statistics for pair formation because the number of nearest neighbors is lower at the surface. However, the fraction of dopant ion pairs is higher in high surface area of nanorod samples than nanoparticle samples for a given concentration. Therefore, upconversion emission intensities are significantly decreased by the dopant pair formation, that is, cross-relaxation nonradiative process. It could be one of the reasons for decreasing the upconversion luminescence intensity in a rod sample. Lattice strain may be one of the reasons behind it because Aumer et al.[26] reported the effects of tensile and compressive strain on the luminescence properties of quantum well structures. In the present study, we have seen that the tensile strain of nanorod (+1.9%) samples is higher than that of nanoparticle (+1.0%) samples and the upconversion luminescence intensity decreases with increasing tensile strain. This indicates that the nonradiative relaxation pathway increases with increasing lattice strain. Therefore, we believe that lattice strain plays an important role in tuning the efficiency of the upconversion luminescence properties of doped nanoparticles.

It is seen from FTIR study (Figure 12) that a larger amount of hydroxyl groups are present at nanorod samples than at nanoparticle samples because of the high surface area. A broad band in the 3400−3700 cm^{-1} region, which is due to water OH stretching vibrations, and the corresponding bending vibration is at 1630 cm^{-1}. In both cases, the peak near 1052 cm^{-1} is split because of the phosphate P−O stretching, and the peaks around 620 cm^{-1} and 540 cm^{-1} correspond to the O=P−O bending and O−P−O bending modes, respectively.[27] Hydroxyl content is another reason for decreasing the upconversion emission intensity in nanorod samples.
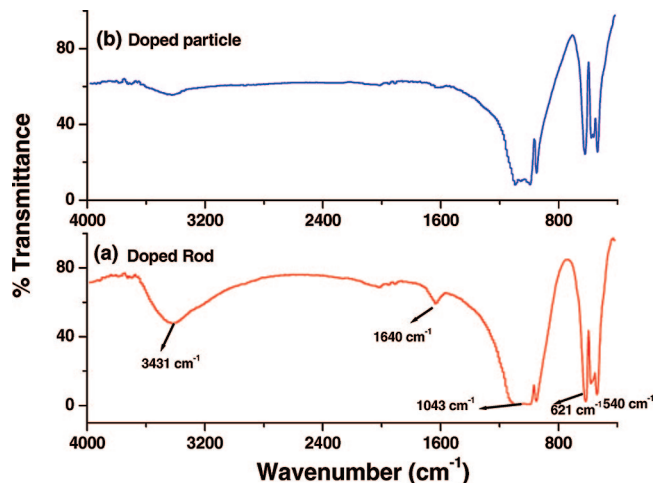
LaPO₄:Er@Yb Core−Shell Nanoparticles/Nanorods

J. Phys. Chem. C, Vol. 112, No. 26, 2008 **9657**

Figure 12. FTIR spectra of (a) 1.0 mol % Er^{3+}- and 1.0 mol % Yb^{3+}-doped rod (900 °C) and (b) 1.0 mol % Er^{3+}- and 1.0 mol% Yb^{3+}-doped particle (900 °C), respectively.

Figure 13. Plot of UPC fluorescence peak intensity (green) against lattice strain of doped particle/rod and core−shell particle/rod and Yb-doped LaPO₄ nanorod.

The enhancement of emission intensity of core−shell LaPO₄: Er@Yb with respect to LaPO₄:Er:Yb -doped nanoparticles/nanorods may be attributed to the fact that a significant amount of nonradiative centers existing on the surface of LaPO₄:Er:Yb nanoparticles/nanorod is eliminated by the shielding effect of the Yb_2O_3 shell. In the core−shell structure, the distance between the dopant ions (Er and Yb) is increased and the surface quenchers are decreased, thus reducing the nonradiative relaxation pathways and suppressing the cross-relaxation quenching due to the energy transfer process. In addition, the removal of surface OH groups due to surface coating also influences the radiative relaxation pathway. In the case of doped nanoparticle and nanorod LaPO₄ samples, the surfaces of these particles are usually covered with hydroxyl groups as well as physisorbed water molecules, and these surface OH groups play a major role in quenching the PL intensity.[20] However, Yb-coated nanoparticles or nanorod samples should have less surface OH⁻ groups because of surface coating. Therefore, the removal of surface OH groups reduces the nonradiative decay. Here, we observed the tensile strain for a doped LaPO₄ particle (+1.0%), whereas compressive strain (−0.37%) is obtained after surface coating. Aumer et al.[26] already reported that the emission intensity increases with decreasing tensile strain. In the present study, we also observed that the upconversion emission intensity increases with surface coating, which again suggests that the upconversion emission intensity increases with decreasing strain. This means that the nonradiative relaxation decreases with decreasing strain from tensile to compressive. All of these reasons will explain the significant increases in the overall luminescence intensity with changing the shape and surface coating. A summary of the results of the corelation between UPC fluorescence intensity and lattice strain is seen in Figure 13. The strain is found to introduce a significant effect on the upconversion properties of the rare-earth-doped and coated nanocrystals. Thus, we may say that the changes observed in the upconversion emission intensity are mainly due to modifications of nonradiative relaxation processes due to surface-related effects.

Conclusions

In conclusion, the solution-based technique is a promising route for the synthesis of LaPO₄:Er:Yb-doped nanoparticles/nanorods and LaPO₄:Er@Yb core−shell nanoparticles/nanorods.
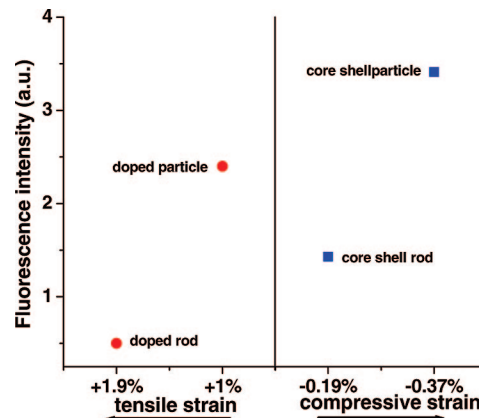
We observed infrared to green and red upconversion in $Er^{3+}−Yb^{3+}$ codoped LaPO₄ nanocrystals under near-infrared radiation (970 nm). Our results highlight that the upconversion emission properties can be tuned by changing the shape and surface coating. We confirmed that the pump power dependence of green and red UPC emission is quadratic, indicating that two-photon excitation processes are involved in the UPC processes. The enhancement of upconversion emission of LaPO₄:Er:Yb doped nanoparticles and LaPO₄:Er@Yb core−shell nanoparticles/nanorods is mainly due to modifications of nonradiative relaxation processes due to surface-related effects. It is seen that the tensile strain varies from +1.0% to +1.9% with changing the shape from nanoparticle to nanorod. However, compressive strain (−0.37%) is obtained after surface coating of the doped nanoparticle (+1.0%). It is worth mentioning that the upconversion emission intensity increases with decreasing tensile strain. The strain was found to introduce significant effects on the upconversion properties of the rare-earth-doped nanocrystals.

Supporting Information Available: Lattice strain for undoped LaPO₄ particle and rod (S1a and b), and strain for 1 mol % Er^{3+}-doped LaPO₄ particle and rod (S2a and b) are analyzed in this part. S3 shows the EDXA of LaPO4:Er@Yb nanocrystals. This information is available free of charge via the Internet at http://pubs.acs.org.

References and Notes

(1) (a) Prasad, P. N. *Nanophotonics;* John Wiley & Sons: New York, 2004. (b) Auzel F., F. *Chem. Rev* **2004**, *104*, 139. (c) Silversmith, A. J.; Lenth, W.; Macfarlane, R. M. *Appl. Phys. Lett.* **1987**, *51*, 1977.

(2) (a) Heer, S.; Kömpe, K.; Güdel, U. H.; and Haase, M. *Adv. Mater.* **2004**, *16*, 2102. (b) Schäfer, H.; Ptacek, P.; Kömpe, K.; Haase, M. *Chem. Mater.* **2007**, *19*, 1396. (c) Patra, A.; Saha, S.; Alentar, R. C. M.; Rakov, N. A.; and Maciel, S. G. *Chem. Phys. Lett.* **2005**, *407*, 477. (d) Patra, A.; Ghosh, P.; Saha Chowdhury, P.; Alentar, R. C. M.; Lozano, B. W.; Rakov, N. A.; and Maciel, S. G. *J. Phys. Chem. B* **2005**, *109*, 10142. (e) Sivakumar, S.; Veggel, V.M.J.C.F.; and Raudsepp, M. *J. Am. Chem. Soc.* **2005**, *127*, 12464. (f) Rosa-Cruz, E. De La,.; Diaz-Torres, L. A.; Rodriguez-Rojas, R. A.; Meneses-Nava, M. A.; Barbosa-Garcia, O.; Salas, P. *Appl. Phys. Lett.* **2003**, *83*, 4903.

(3) (a) Wang, X.; Kong, X.; Shan, G.; Yu, Y. I.; Sun, Y.; Feng, L.; Chao, K.; Lu, S.; and Li, Y. *J. Phys. Chem. B.* **2004**, *108*, 18408. (b) Guo, H.; Dong, N.; Yin, M.; Zhang, W.; Lou, L.; and Xia, S. *J. Phys. Chem. B* **2004**, *108*, 19205. (c) Chen, W.; Joly, G. A.; Zhang, Z. *J. Phys. Rev. B* **2001**, *64*, 041202.

9658 *J. Phys. Chem. C, Vol. 112, No. 26, 2008*

Ghosh et al.

(4) Wang, L.; Yan, R.; Huo, Z.; Wang, L.; Zeng, J.; Wang, X.; Peng, Q.; Li, Y. *Angew. Chem., Int. Ed.* **2005**, *44*, 6054.

(5) (a) Niedbala, A. R. S.; Feindt, H.; Kordos, K.; Vail, T.; Burton, J.; Bielska, B.; Li, S.; Milunic, D.; Bourdelle, P.; and Vallejo, R. *Anal. Biochem.* **2001**, *293*, 22. (b) Soukka, T.; Kuningas, K.; Rantanen, T.; Haaslahti, V.; Lovgren, T. *J. Fluoresc.* **2005**, *15*, 513. (c) Yuan, J.; Wang, G. *Trends Anal. Chem.* **2006**, *25*, 490.

(6) (a) Rijke, F.; Zijlmans, H.; Li, S.; Vail, T.; Raap, A. K.; Niedbala, R. S.; Tanke, H. J. *Nat. Biotechnol.* **2001**, *19*, 273. (b) Corstjens, P.; Zuiderwijk, M.; Brink, A.; Li, S.; Feindt, H.; Niedbala, R. S.; Tanke, H. J. *Clin. Chem.* **2001**, *47*, 1885. (c) Hampl, J.; Hall, M.; Mufti, N. A.; Yao, Y. M.; MacQueen, D. B.; Wright, W. H.; Cooper, D. E. *Anal. Biochem.* **2001**, *288*, 176.

(7) Heer, S.; Lehmann, O.; Haase, M.; Güdel, H. U. *Angew. Chem., Int. Ed.* **2003**, *42*, 3179.

(8) Meiser, F.; Cortez, C.; Caruso, F. *Angew. Chem., Int. Ed.* **2004**, *43*, 5954.

(9) (a) Patra, A.; Friend, C. S.; Kapoor, R.; Prasad, P. N. *Appl. Phys. Lett.* **2003**, *83*, 284. (b) Patra, A.; Friend, C. S.; Kapoor, R.; Prasad, P. N. *J. Phys. Chem. B* **2002**, *106*, 1909.

(10) (a) Lehmann, O.; Kömpe, K.; Haase, M. *J. Am. Chem. Soc.* **2004**, *126*, 14935. (b) Song, H.; Yu, L.; Lu, S.; Wang, T.; Liu, Z.; Yang, L. *Appl. Phys. Lett.* **2004**, *85*, 470. (c) Buissette, V.; Moreau, M.; Gacoin, T.; Boilot, P. J.; Ching, C. T. J.; Mercier, L. T. *Chem. Mater.* **2004**, *16*, 3767. (d) Stouwdam, W. J.; Veggel, V. M. J. C. F. *Langmuir* **2004**, *20*, 11763. (e) Yu, L.; Song, H.; Lu, S.; Liu, Z.; Yang, L.; Kong, X. *J. Phys. Chem. B* **2004**, *108*, 16697.

(11) Kömpe, K.; Borchert, H.; Storz, J.; Lobo, A.; Adam, S.; Möller, T.; Haase, M. *Angew. Chem., Int. Ed.* **2003**, *42*, 5513.

(12) Mullica, F. D.; Milligan, O. W.; Grossie, A. D.; Beall, W. G.; Boatner, A. L. *Inorg. Chim. Acta* **1984**, *95*, 231.

(13) Zhang, W. Y.; Yan, G. Z.; You, P. L.; Si, R.; Yan, H. C. *Eur. J. Inorg. Chem.* **2003**, *22*, 4099.

(14) Vegard, L. *Z. Phys.* **1921**, *5*, 17.

(15) Liang, L.; Wu, H.; Hu, H.; Wu, M.; Su, Q. *J. Alloys Compd.* **2004**, *368*, 94.

(16) Li, W.; Frenkel, I. A.; Woicik, C. J.; Ni, C.; Shah, I. S. *Phys. Rev. B* **2005**, *72*, 155315.

(17) Shanon, D. R. *Acta Crystallogr.* **1976**, *32*, 751.

(18) Yu, R.; Jonghe, De, C, L. *J. Phys. Chem. C* **2007**, *111*, 11003.

(19) Williamson, K. G.; Hall, H. W. *Acta Metall.* **1953**, *1*, 32.

(20) Ghosh, P.; Patra, A. *J. Phys. Chem. C* **2007**, *111*, 7004.

(21) Penn, L. R.; Banfield, F. J. *Science* **1998**, *281*, 969.

(22) Peng, Z. A.; Peng, X. G. *J. Am. Chem. Soc* **2001**, *123*, 1389.

(23) Peng, Z. A.; Peng, X. G. *J. Am. Chem. Soc* **2002**, *124*, 3343.

(24) Fang, P. Y.; Xu, W. A.; Song, Q. R.; Zhang, X. H.; You, P. L.; Yu, C. J.; Liu, Q. H. *J. Am. Chem. Soc* **2003**, *125*, 16025.

(25) Cao, M.; Hu, C.; Wu, Q.; Guo, C.; Qi, Y.; Wang, E. *Nanotechnology* **2005**, *16*, 282.

(26) Aumer, M. E.; LeBoeuf, S. F.; Bedair, S. M.; Smith, M.; Lin, J. Y.; Jian, H. X. *Appl. Phys. Lett.* **2000**, *77*, 821.

(27) Bo, L.; Liya, S.; Xiaozhen, L.; Shuiche, Z.; Yumeri, Z.; Tianmain, W.; Sasaki, Y.; Ishii, K.; Kashiwaya, Y.; Takahashi, H.; Shibayama, T. *J. Mater. Sci. Lett.* **2001**, *20*, 1071.